Kinematic reconstruction of atmospheric neutrino events in a large water Cherenkov detector with proton identification

M. Fechner,[10,*] K. Abe,[1] Y. Hayato,[1,3] T. Iida,[1] M. Ikeda,[1] J. Kameda,[1] K. Kobayashi,[1] Y. Koshio,[1] M. Miura,[1] S. Moriyama,[1,3] M. Nakahata,[1,3] S. Nakayama,[1] Y. Obayashi,[1] H. Ogawa,[1] H. Sekiya,[1] M. Shiozawa,[1,3] Y. Suzuki,[1,3] A. Takeda,[1] Y. Takenaga,[1] Y. Takeuchi,[1,3] K. Ueno,[1] K. Ueshima,[1] H. Watanabe,[1] S. Yamada,[1] S. Hazama,[2] I. Higuchi,[2] C. Ishihara,[2] T. Kajita,[2,3] K. Kaneyuki,[2,3] G. Mitsuka,[2] H. Nishino,[2] K. Okumura,[2] N. Tanimoto,[2] M. R. Vagins,[3,7] F. Dufour,[4] E. Kearns,[4,3] M. Litos,[4] J. L. Raaf,[4] J. L. Stone,[4,3] L. R. Sulak,[4] W. Wang,[4] M. Goldhaber,[5] S. Dazeley,[6] R. Svoboda,[6] K. Bayes,[7] D. Casper,[7] J. P. Cravens,[7] W. R. Kropp,[7] S. Mine,[7] C. Regis,[7] M. B. Smy,[7,3] H. W. Sobel,[7,3] K. S. Ganezer,[8] J. Hill,[8] W. E. Keig,[8] J. S. Jang,[9] J. Y. Kim,[9] I. T. Lim,[9] K. Scholberg,[10,3] C. W. Walter,[10,3] R. Wendell,[10] S. Tasaka,[11] J. G. Learned,[12] S. Matsuno,[12] Y. Watanabe,[13] T. Hasegawa,[14] T. Ishida,[14] T. Ishii,[14] T. Kobayashi,[14] T. Nakadaira,[14] K. Nakamura,[14,3] K. Nishikawa,[14] Y. Oyama,[14] K. Sakashita,[14] T. Sekiguchi,[14] T. Tsukamoto,[14] A. T. Suzuki,[15] A. Minamino,[16] T. Nakaya,[16,3] M. Yokoyama,[16] Y. Fukuda,[17] Y. Itow,[18] T. Tanaka,[18] C. K. Jung,[19] G. Lopez,[19] C. McGrew,[19] R. Terri,[19] C. Yanagisawa,[19] N. Tamura,[20] Y. Idehara,[21] M. Sakuda,[21] Y. Kuno,[22] M. Yoshida,[22] S. B. Kim,[23] B. S. Yang,[23] T. Ishizuka,[24] H. Okazawa,[25] Y. Choi,[26] H. K. Seo,[26] Y. Furuse,[27] K. Nishijima,[27] Y. Yokosawa,[27] M. Koshiba,[28] Y. Totsuka,[28,†] S. Chen,[29] Y. Heng,[29] Z. Yang,[29] H. Zhang,[29] D. Kielczewska,[30] E. Thrane,[31,‡] and R. J. Wilkes[31]

(Super-Kamiokande Collaboration)

[1]*Kamioka Observatory, Institute for Cosmic Ray Research, University of Tokyo, Kamioka, Gifu 506-1205, Japan*
[2]*Research Center for Cosmic Neutrinos, Institute for Cosmic Ray Research, University of Tokyo, Kashiwa, Chiba 277-8582, Japan*
[3]*Institute for the Physics and Mathematics of the Universe, University of Tokyo, Kashiwa, Chiba 277-8582, Japan*
[4]*Department of Physics, Boston University, Boston, Massachusetts 02215, USA*
[5]*Physics Department, Brookhaven National Laboratory, Upton, New York 11973, USA*
[6]*Department of Physics, University of California, Davis, California 95616, USA*
[7]*Department of Physics and Astronomy, University of California, Irvine, Irvine, California 92697-4575, USA*
[8]*Department of Physics, California State University, Dominguez Hills, Carson, California 90747, USA*
[9]*Department of Physics, Chonnam National University, Kwangju 500-757, Korea*
[10]*Department of Physics, Duke University, Durham, North Carolina 27708, USA*
[11]*Department of Physics, Gifu University, Gifu, Gifu 501-1193, Japan*
[12]*Department of Physics and Astronomy, University of Hawaii, Honolulu, Hawaii 96822, USA*
[13]*Physics Division, Department of Engineering, Kanagawa University, Kanagawa, Yokohama 221-8686, Japan*
[14]*High Energy Accelerator Research Organization (KEK), Tsukuba, Ibaraki 305-0801, Japan*
[15]*Department of Physics, Kobe University, Kobe, Hyogo 657-8501, Japan*
[16]*Department of Physics, Kyoto University, Kyoto, Kyoto 606-8502, Japan*
[17]*Department of Physics, Miyagi University of Education, Sendai, Miyagi 980-0845, Japan*
[18]*Solar Terrestrial Environment Laboratory, Nagoya University, Nagoya, Aichi 464-8602, Japan*
[19]*Department of Physics and Astronomy, State University of New York, Stony Brook, New York 11794-3800, USA*
[20]*Department of Physics, Niigata University, Niigata, Niigata 950-2181, Japan*
[21]*Department of Physics, Okayama University, Okayama, Okayama 700-8530, Japan*
[22]*Department of Physics, Osaka University, Toyonaka, Osaka 560-0043, Japan*
[23]*Department of Physics, Seoul National University, Seoul 151-742, Korea*
[24]*Department of Systems Engineering, Shizuoka University, Hamamatsu, Shizuoka 432-8561, Japan*
[25]*Department of Informatics in Social Welfare, Shizuoka University of Welfare, Yaizu, Shizuoka, 425-8611, Japan*
[26]*Department of Physics, Sungkyunkwan University, Suwon 440-746, Korea*
[27]*Department of Physics, Tokai University, Hiratsuka, Kanagawa 259-1292, Japan*
[28]*The University of Tokyo, Bunkyo, Tokyo 113-0033, Japan*
[29]*Department of Engineering Physics, Tsinghua University, Beijing, 100084, China*
[30]*Institute of Experimental Physics, Warsaw University, 00-681 Warsaw, Poland*
[31]*Department of Physics, University of Washington, Seattle, Washington 98195-1560, USA*
(Received 13 January 2009; published 22 June 2009)

[*]Present address: CEA, Irfu, SPP, Centre de Saclay, F-91191, Gif-sur-Yvette, France.
[†]Deceased.
[‡]Present address: Department of Physics and Astronomy, University of Minnesota, MN, 55455, USA.

We report the development of a proton identification method for the Super-Kamiokande (SK) detector. This new tool is applied to the search for events with a single proton track, a high purity neutral current sample of interest for sterile neutrino searches. After selection using a neural network, we observe 38 events in the combined SK-I and SK-II data corresponding to 22 85.1 days of exposure, with an estimated signal-to-background ratio of 1.6 to 1. Proton identification was also applied to a direct search for charged-current quasielastic (CCQE) events, obtaining a high precision sample of fully kinematically reconstructed atmospheric neutrinos, which has not been previously reported in water Cherenkov detectors. The CCQE fraction of this sample is 55%, and its neutrino (as opposed to antineutrino) fraction is $91.7 \pm 3\%$. We selected 78 μ-like and 47 e-like events in the SK-I and SK-II data set. With this data, a clear zenith angle distortion of the neutrino direction itself is reported in a sub-GeV sample of μ neutrinos where the lepton angular correlation to the incoming neutrino is weak. Our fit to $\nu_\mu \rightarrow \nu_\tau$ oscillations using the neutrino $\frac{L}{E}$ distribution of the CCQE sample alone yields a wide acceptance region compatible with our previous results and excludes the no-oscillation hypothesis at 3-sigma.

DOI: 10.1103/PhysRevD.79.112010 PACS numbers: 14.60.Pq, 14.60.St, 29.40.Ka

I. INTRODUCTION

The Super-Kamiokande detector is well known for its discovery of atmospheric neutrino oscillations. It is a large, 50-kton, cylindrical water Cherenkov detector located under Mt. Ikenoyama near Kamioka, Japan [1]. It is separated in two concentric regions: a 2 m-thick outer veto (outer detector or OD), instrumented with 1885 8 in. photomultiplier tubes (PMTs) facing outward, used as a cosmic ray veto; and an inner detector (ID) instrumented with 11 146 inward facing 20 in. PMTs. The Cherenkov light emitted by charged particles traveling in the water travels to the walls and the resulting ring-shaped patterns are then analyzed.

Super-Kamiokande has very good particle identification (PID) capabilities, being able to separate muon tracks from electron tracks with better than 1.8% misidentification [2]. Until now, no attempt has been made to extend its PID algorithm to other types of particles produced in neutrino interactions. In this article we demonstrate that Super-Kamiokande can also be used to search for proton tracks. Other authors have published estimates predicting what would be found in Super-Kamiokande and other experiments, along with explorations of the physics consequences [3].

This improved PID technique will be described in Sec. II B. In Sec. III we will describe atmospheric neutrino data selection and reconstruction at Super-Kamiokande. In Sec. IV we will apply this new proton selection algorithm to a search for neutral current (NC) elastic $\nu + p \rightarrow \nu + p$ events. This sample has high neutral current purity and angular correlation with the incoming neutrino, and is potentially sensitive to $\nu_\mu \rightarrow \nu_{\text{sterile}}$ oscillations [3].

In Sec. V we will extend the technique to charged-current quasielastic (CCQE) neutrino interactions, reconstructing both the outgoing lepton and the proton. This allows full kinematic reconstruction of the atmospheric neutrino track, improving neutrino zenith angle, flight length, and energy reconstruction, which is useful for oscillation studies. This is the first time such a reconstruction has been performed in a water Cherenkov detector.

II. A PROTON TRACK FITTER FOR SUPER-KAMIOKANDE

A. Characteristics of proton tracks in Super-Kamiokande

Proton tracks in water exhibit certain features that make it possible to identify them.

The main parameter in Cherenkov light production is the velocity β of the particle, related to the Cherenkov cone opening angle by

$$\cos\theta = \frac{1}{\beta n},$$

where n is the refraction index of the medium. In water this leads to a threshold of $\beta \approx 0.74$. Because of the large proton mass this corresponds to a momentum threshold of 1.07 GeV/c. Because of the falling energy spectrum of atmospheric neutrinos, we do not expect to see many proton tracks above 3 GeV/c, corresponding to $\beta < 0.96$. Consequently for most of the protons seen in Super-Kamiokande the half-opening angle of the Cherenkov cone will be relatively small, below about 38°. This contrasts with electrons and muons which have lower mass, and so reach $\beta \approx 1$ and Cherenkov angles of $\approx 42°$ at much lower momenta than protons.

Super-Kamiokande's PID program uses the ring topology to separate muons and electrons: due to scattering and radiative processes creating electromagnetic showers, the outer edges of electron rings are blurred, while muons have rings with sharp outer edges [2]. Like muons, protons will have rings with sharp outer edges. Since muons at these momenta lose their energy by ionization, their ranges are long (typically several meters), leading to thick projected rings on the detector walls. However protons have a high probability of undergoing nuclear interactions with ^{16}O or H nuclei in the water. A large fraction of the time, neither

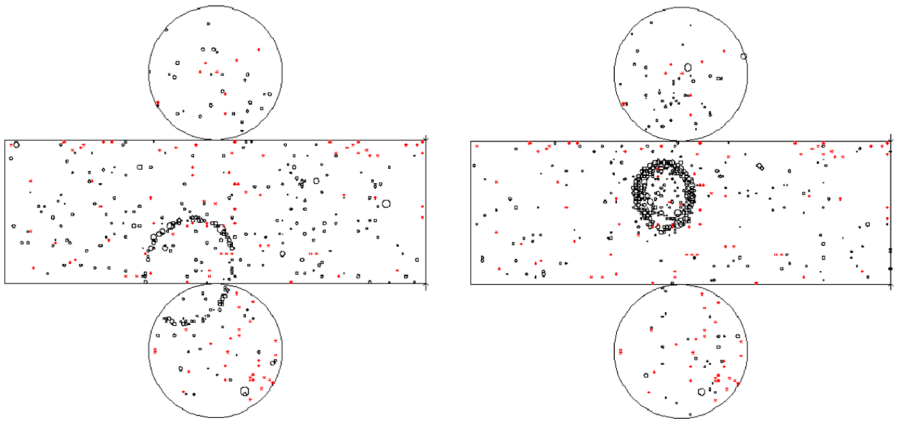

FIG. 1 (color online). Event displays of a Monte-Carlo NC elastic event, with proton momentum of 1490 MeV/c (left), and a Monte-Carlo 300 MeV/c muon. The proton stopped early, causing a thin ring pattern on the wall. The muon ring is thicker than most proton rings with similar opening angles.

the proton nor the secondary particles produced in these collisions are above Cherenkov threshold: in this case the proton's Cherenkov light emission is seen to stop suddenly, causing a short, thin ring to appear on the detector wall. Figure 1 shows typical proton and muon event displays.

Proton tracks have an additional characteristic: as shown in Fig. 2, the probability for a proton to produce a π^0 or a charged secondary during a hadronic interaction in the water increases with momentum, reaching ~50% at around 2 GeV/c based on our Monte-Carlo studies. In particular, if a π^0 is produced, at least one bright electron-like ring (from neutral pion decay gamma showers) will be seen in Super-Kamiokande, greatly reducing the chances of identifying the proton and accurately reconstructing the event. The fraction of protons that do not produce any visible secondary particles goes from ~90% at 1.2 GeV/c to ~40% at 2 GeV/c.

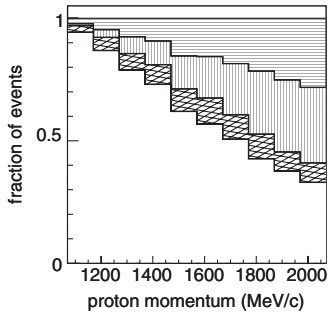

FIG. 2. Probability of hadronic interactions in the water as a function of proton momentum. The clear region shows the fraction of protons that do not interact hadronically in the water. The crosshatched region shows events whose interactions produce only subthreshold secondaries. The region with a vertical hatch pattern corresponds to production of above-threshold charged secondaries, with no π^0. The horizontally hatched region shows the amount of π^0 production.

B. Expected light pattern engine and fitter

Particle identification is a hypothesis test, and is dealt with by calculating a ratio of maximum likelihoods. This is attempted after a previous fitter has already computed a vertex position, Cherenkov opening angle, and candidate ring direction. A *light pattern engine* generates the average Cherenkov pattern corresponding to the given vertex and track configuration inside the tank. Depending on the hypothesis being tested, several parameters of the Cherenkov cone are then adjusted to maximize a *pattern likelihood* built from the observed and expected charges on individual phototubes. This procedure is carried out twice, using the two different particle types that are being studied to generate the light patterns. In this analysis, a special particle identification algorithm that takes into account protonlike features was developed. During the first stage, we assume the ring was created by a proton, and during the second stage it is assumed to be a muon. We will now briefly describe the light pattern engine as well as the fit performed during the proton hypothesis test.

1. Calculation of expected charge patterns

Expected light patterns are produced using a program described in [4]. For proton identification we have extended the program's capabilities. Using a GEANT4 [5] Monte-Carlo simulator, we obtained tables of the Cherenkov photon density

$$\frac{d^3N}{drdpd\cos\theta},$$

where r is the distance from the vertex, p is the particle momentum. and θ is the angle with respect to the particle track (cone axis). This table was built in "pure" water, i.e. all scattering and absorption effects were turned off; moreover, proton hadronic interactions and δ-ray production were turned off, but energy loss by ionization was kept. Thirty batches of monochromatic protons at momenta from

1.1 to 4.0 GeV/c were used, with 50 MeV/c spacing until 1.5 GeV/c, 100 MeV/c spacing until 3500 MeV/c, and one batch at 4 GeV/c. The distance r was sampled every 50 cm. We used 400 bins in $\cos\theta$ from 1 to 0.6 to sample the edge of the Cherenkov ring as finely as possible.

For a given vertex, track direction, and momentum p, the amount of Cherenkov light on a given phototube is calculated by linear interpolation from this table. The computed photon flux is azimuthally symmetric around the proton track. PMT solid angle and acceptance corrections, water attenuation, and scattering effects are then applied to the light pattern. Since the photon flux is tabulated at fixed momenta, the Cherenkov opening angle of the cone is quantized in relatively large steps; consequently before any interpolation is done, each $\frac{d^2N}{drd\cos\theta}$ distribution is reweighted so that its peak angle matches the Cherenkov angle at input momentum p to avoid any numerical problems.

As explained earlier, one of the main features of protons is that their Cherenkov light emission can be stopped suddenly in the water. The pattern engine was modified to produce light patterns for any path length: stopping the path length is simulated by masking the PMTs inside the inner edge of the cone. A smooth cubic spline is used to describe the effects of finite PMT size for PMTs just on the edge of the lit region.

A MINUIT-based fit [6] was built to fit the observed light pattern with an expected light pattern. The free parameters in the fit are the proton momentum and proton track length.

The expected light pattern then needs to be normalized. The relevant variable in Super-Kamiokande is $R_{\rm tot}$, the amount of photoelectrons collected in a 70° cone around the track, correcting for water attenuation and scattering as well as PMT acceptance [7]. For electrons and muons, tables linking the particle momentum to $R_{\rm tot}$ are used for momentum determination throughout the reconstruction. For protons, a one-to-one conversion function does not exist since protons may stop abruptly in the water, yielding the same amount of light for different initial momenta. Using Super-Kamiokande's Monte-Carlo simulation with hadronic interactions turned off, conversion tables from proton momentum to $R_{\rm tot}^{\rm max}$, the maximum achievable value, were calculated. The proton average track length without hadronic interactions, $L_{\rm max}$, was also obtained in this way. Then, by simulating batches of protons at fixed path lengths, it was found that $\frac{R_{\rm tot}}{R_{\rm tot}^{\rm max}}$ is only a function of $\frac{L}{L_{\rm max}}$ and not of the initial momentum of the proton. Figure 3 shows this function as well as a fit. These calculations allow us to renormalize the expected light pattern to its expected $R_{\rm tot}(l, p)$ value for any given input length l and momentum p, ensuring that the maximum likelihood fit is well behaved.

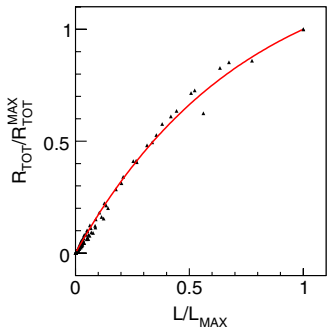

FIG. 3 (color online). $\frac{R_{\rm tot}}{R_{\rm tot}^{\rm max}}$ as a function of $\frac{L}{L_{\rm max}}$ for Monte-Carlo batches at different momenta and fixed path lengths in the detector. The solid (red) line shows the best fit to the functional form $a(\exp(-b\frac{L}{L_{\rm max}}) - 1)$, with $a = -1.29$ and $b = 1.5$. The function allows one to calculate the expected amount of light for any proton pattern.

The fitter returns the maximum likelihood $L_{\rm proton}$, as well as the protonlike momentum and protonlike length of the event. In a separate stage, $L_{\rm muon}$, the likelihood that the pattern is muonlike is calculated.

C. Performance of the proton fitter

The performance of this new algorithm has been tested using Monte-Carlo samples of muons, protons, and charged pions. The samples were produced using GEANT3 and include full fluctuations of all processes and other detector effects. The momentum resolution for protons varies from about 3% below 1.5 GeV/c, to about 10% at 2 GeV/c, reaching 30% at 2.5 GeV/c. The mean resolution of the momentum fit over the NC elastic proton spectrum (for the atmospheric neutrino spectrum) is about 7%, with a small positive bias in the momentum determination of 3%. The resolution gets worse as the momentum increases because it is mostly controlled by the opening angle measurement of the Cherenkov ring. As the angle increases, small variations in the angle measurement result in larger changes in the fitted momentum. Figure 4 summarizes the results of momentum reconstruction.

Figure 5 shows the distributions of the fitted path lengths for monoenergetic simulated protons for two different momenta. At low energy, the distribution has a sharp peak at higher values, corresponding to protons that trav-

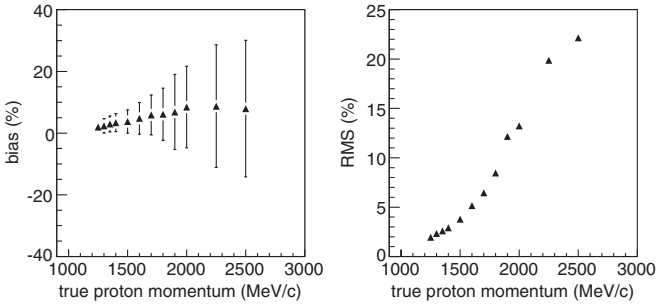

FIG. 4. Bias (left) and root-mean-square (right) of proton momentum reconstruction, using monochromatic Monte-Carlo.

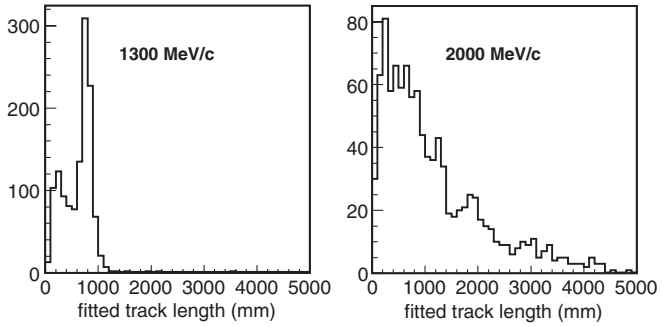

FIG. 5. Fitted track length for Monte-Carlo protons at 1.3 and 2.0 GeV/c. At 2.0 GeV/c the protons never reach their maximum path length.

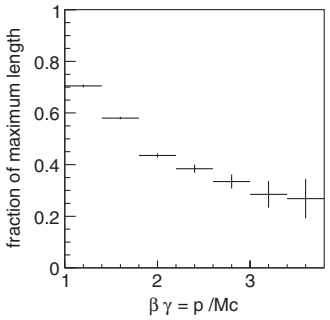

FIG. 6. Average fraction of the maximum path length in water, traveled in water as a function of proton momentum (estimated with NC elastic Monte-Carlo events). The effect of hadronic interactions is clear.

eled their full path-length (no interaction in the water), and a region at lower fitted track lengths corresponding to proton tracks that stopped early. At higher input momenta all protons traveled less than their maximum path length and the distribution falls off. This observation of hadronic interactions in the water can be summarized as the average ratio $\frac{L}{L_{\max}}$ as a function of the input value of $\beta\gamma$. Figure 6 shows that the ratio clearly decreases with input proton momentum, showing the increase of the hadronic cross section with momentum.

III. THE SUPER-KAMIOKANDE ATMOSPHERIC DATA SET

A. Fully-contained atmospheric data

The data used in this paper were collected at Super-Kamiokande during two separate run periods. The first one, labeled SK-I, ran from April 1996 to July 2001, with 40% photocathode coverage (11 146 ID PMTs). The second one, called SK-II, ran from September 2002 to October 2005, with 19% photocathode coverage (5183 ID PMTs), as a result of partial reconstruction following an accident that occurred in November 2001. In SK-II the PMTs were encased in a protective fiberglass shell with a transparent acrylic window to protect against the risk of tube implosion. The two data sets, respectively, correspond to 1489.2 and 798.6 integrated days of livetime.

Super-Kamiokande data first undergo a reduction process, which selects atmospheric neutrino events and splits them into separate samples and eliminates backgrounds. In this paper, the only relevant sample is the fully-contained (FC) data set, since protons have relatively short tracks in the water and do not escape the tank. The purpose of FC reduction is to remove events entering the detector—mainly downward-going cosmic ray muons—as well as events caused by flashing PMTs, and events with tracks escaping the inner detector. The optical separation between the inner detector (ID) and the outer detector (OD) is used during this process. Details of the reduction process can be found in [2].

B. Event reconstruction

Fully-contained data are then fitted by a series of programs which find the vertex and particle tracks. Details about the reconstruction can be found in [2,7]. The initial step is to obtain a starting vertex and track direction using timing information only. PMTs on the edge of the brightest Cherenkov ring are then identified. The method for tagging edge PMT, and Cherenkov opening angle measurement, is different in SK-I and SK-II. In SK-I, the distribution $Q(\theta)$ of observed charges as a function of opening angle is constructed. The edge of the ring is taken to be the first zero of the second derivative $\frac{d^2Q}{d\theta^2}$ occurring after the maximum of Q. In SK-II, with half the photocoverage, the sampling of $Q(\theta)$ was found to be too low for an accurate determination of the derivatives; therefore, a method based on light patterns is used. The expected light pattern of a Cherenkov ring (e or μ) is fit to the observed pattern, allowing its opening angle to vary; the edge of the ring is found at the best fit, and edge PMTs are then tagged.

Once edge PMTs are tagged, they are used to refine the Cherenkov ring direction. An estimated track length is calculated, and the vertex position is changed by maximizing an estimator based on PMT timing and charge, treating PMTs inside and outside of the Cherenkov edge differently. This procedure is iterated until a stable vertex and direction are found. The next step is to search for other rings in the event.

A Hough transform method [8] is used to look for possible ring candidates. A pattern likelihood function is built to determine whether adding each Hough seed matches the observed charge pattern better. Other estimators involving the charge density in the candidate ring are also considered. If a better match is found by adding a ring, the seed is added to the list of tracks. This procedure is iterated until a maximum of 5 rings is found.

The next step is particle identification (PID): each observed ring is compared to a muon pattern and an electron pattern using a likelihood method, and is then assigned a particle type, either e-like or μ-like. After PID, single-ring

events are processed by a refined track fitter that uses PID information to improve the vertex and track fit.

An important variable is the *visible energy*, which is the energy of an electron that would cause the same amount of light in the tank. It is estimated at the end of the reconstruction process.

The performances of PID and the refined vertex fitter are not optimal for proton tracks, since by design the particle is assumed to be a lepton in these algorithms. In the search for NC elastic events described in the present section we do not use the results of these two algorithms. However, for the analysis described in Sec. V we do apply them.

C. Monte-Carlo simulation

Monte-Carlo simulation of atmospheric neutrino events in Super-Kamiokande relies on three successive steps:

(1) *Atmospheric neutrino flux determination*: the model by Honda *et al.*[9] is used in this paper.

(2) *Simulation of neutrino interactions in the water*: Two different programs were used: the NEUT simulation [10] and the NUANCE (version 3) [11] simulation. Details about NEUT are also available in [2]. The versions used in this paper include rescattering of the outgoing nucleons, which is relevant for estimating the number of protons expected above Cherenkov threshold. Both NEUT and NUANCE assume the axial-vector form factor to have a dipole shape, with the axial mass set to 1.21 GeV (for CCQE and charged-current [CC] single-pion interactions).

(3) *Tracking of interaction products in Super-Kamiokande*: A complete simulation of Super-Kamiokande using the GEANT3 [12] package is used. The Cherenkov light production and propagation models have been tuned to calibration data [1]. In addition, careful studies of the reflection of light on the acrylic surfaces, PMT glass, and plastic lining of the tank have been carried out. The output of the GEANT3 simulation is in the same format as the data, and undergoes the same reduction and fitting process. The events are reweighted for livetime, solar wind activity, and for $\nu_\mu \rightarrow \nu_\tau$ neutrino oscillations.

IV. SEARCH FOR NC ELASTIC $\nu + p \rightarrow \nu + p$ EVENTS IN SUPER-KAMIOKANDE ATMOSPHERIC DATA

The first application of the proton fitter described above is to search for single-ring proton events caused by the neutral current elastic interaction $\nu + p \rightarrow \nu + p$.

A. Single proton selection

We initially select a sample of fully-contained (or FC) atmospheric events, with their vertices (calculated by the initial fitter) more than 2 m away from the wall, which defines a 22.5 kton fiducial volume (FV). We also require that there be only one ring. The vertex resolution—defined as the radius of the sphere centered on the true vertex that contains 68.3% of reconstructed vertices—for single proton tracks from simulated atmospheric NC elastic events is estimated to be $\sim$85 cm, with an angular resolution of $\sim 2.8^\circ$ on the reconstructed direction. The Cherenkov angle is measured with an accuracy of $\sim 1.6^\circ$, with a bias of -1.4°.

We estimate that 7.0 visible NC elastic interactions occur every year in the fiducial volume. These are events for which proton NC elastic collisions produced a single outgoing proton above threshold which in turn produced no visible secondary in hadronic collisions in the water.

However, other interaction modes create similar events with a single visible proton, especially neutral current single-pion (NC1π) events where the pion is absorbed; and NC elastic collisions on neutrons where the neutron produces a proton above Cherenkov threshold through hadronic collisions. Using Monte-Carlo information, we determined that 5.9 such events are produced per year in the fiducial volume, for a total of 12.9 single visible protons per year. Of those, 11.4 (88%) events are fitted as one-ring events with their vertex inside the fiducial volume by our reconstruction. In the remainder of this section we explain how to separate these fitted events from the large backgrounds using the proton identification tool described in Sec. II B.

1. Removal of low energy backgrounds

In atmospheric neutrino analyses, data with less than 30 MeV of visible energy are discarded; they are not used for oscillation searches. However in the present analysis such a reduction cut is too stringent and would remove about 20% of visible protons. At visible energies below 30 MeV, the FC atmospheric neutrino sample does contain neutrino interactions, but also low energy backgrounds, especially spallation events. These are radioactive β decays of fragments left over from the collisions of cosmic ray muons with ^{16}O nuclei in the water. We use the spallation removal technique used in solar neutrino searches, which is described in detail in [13]. Spallation events are correlated in time and space with one of the previous cosmic ray muon tracks; there is also a correlation with muon energy.

As in the solar analysis, a likelihood function based on these three parameters was built. The vertex position and event time of each FC event is checked against all the cosmic ray muons occurring during the previous 100 s, and the highest value of the likelihood is saved. For SK-I, two different likelihood functions are used, depending on the success or failure of the cosmic ray muon track fit. For SK-II both likelihoods were merged into one. Cuts on the likelihood value were chosen to remove the events with a

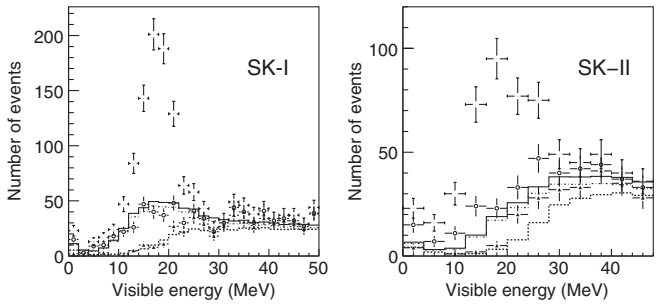

FIG. 7. Visible energy distribution for data and MC single-ring FC events for SK-I and SK-II is shown with no spallation cuts applied (crosses), after the spallation cut (open circles), and after the sparse ring cut (triangles). The corresponding MC distributions are shown (solid line: no cuts; dash-dotted line: only the spallation inefficiency is applied; thick dashed line: the sparse ring cut and spallation inefficiency are applied). Spallation events are present only in the data.

high correlation with a preceding muon. This cut was only applied if $E_{\rm vis} < 50$ MeV. Using real muon data and uniformly distributed times and vertices, we determined that these cuts incur a 8.2% (9.1%) inefficiency on nonspallation atmospheric neutrino events in SK-I (SK-II) below 50 MeV. We also removed 2.7 days of livetime from the SK-I sample when performing the spallation cut because of missing cosmic ray muon data. The values of the cuts and induced inefficiencies differ from those in [13] because we are looking at atmospheric events after fully-contained reduction and vertex reconstruction, and not low energy data after solar neutrino reduction.

In addition, an extra cut was developed to remove some remaining low energy events with a sparse ring, i.e. an incomplete Cherenkov ring pattern. Using the fitted vertex and direction, a 6°-wide annulus was constructed around the Cherenkov ring, and binned in the azimuthal direction in 36 ϕ bins. A sparse ring will have empty ϕ bins, and the average charge per bin will be low. A two-dimensional cut on events with an average charge of less 1 (0.5) pe and more than 15 (22) empty ϕ bins in SK-I (SK-II) was applied. Studies show that this cut improves signal-to-background significance at later stages. Good agreement between data and Monte-Carlo simulation (MC) is reached once the low energy backgrounds are removed, as can be seen in Fig. 7.

2. Proton track selection

After the spallation and sparse ring removal cuts, three selection criteria are applied on the sample to select proton events:

(1) Events with more than 200 MeV of visible energy are discarded. This removes the bulk of the events used for the usual atmospheric analyses, caused by high energy muon or electron tracks.
(2) Events with a Cherenkov opening angle greater than 37° (35° in SK-II) are rejected. This effectively removes high energy muons, as well as showers caused by electrons or γ rays from π^0 decays.
(3) Finally, the pattern likelihood difference calculated by the proton fitter described in Sec. II, viz.

$$\Delta \log L = \log(L_{\rm proton}) - \log(L_{\rm muon}),$$

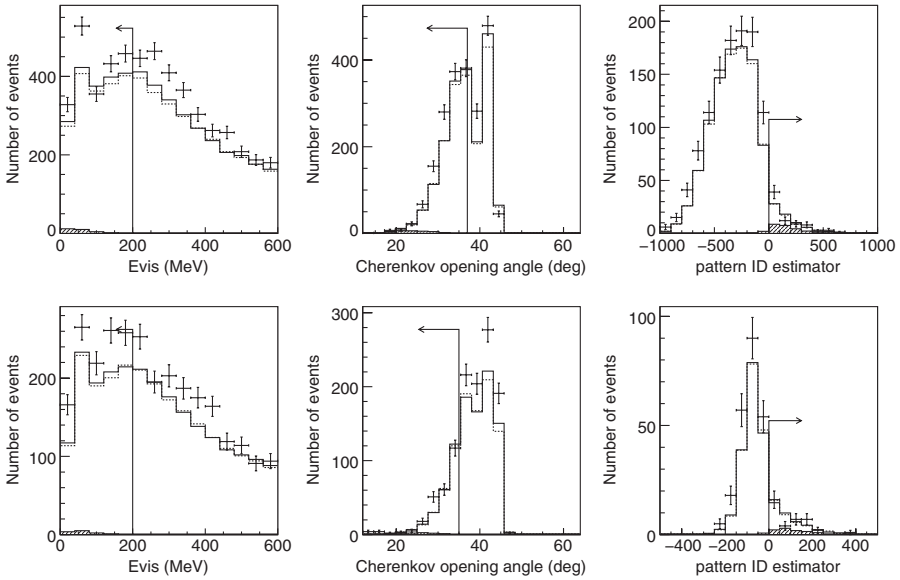

FIG. 8. Distribution of the visible energy, Cherenkov opening angle, and proton pattern likelihood for single-ring events after spallation and sparse ring removal, for SK-I (top row) and SK-II (bottom row). The solid and dashed lines show Monte-Carlo expectation from NEUT and NUANCE, with oscillation reweighting, but no correction for the absolute flux normalization. The hatched histogram shows the fraction of signal events according to NEUT.

TABLE I. Summary of SK-I NC elastic selection. In this table the Monte-Carlo has been reweighted according to livetime, solar activity for SK-I, as well as neutrino oscillations assuming $\Delta m^2 = 2.5 \times 10^{-3}$ eV^2 and $\sin^2 2\theta = 1$. Both NEUT and NUANCE simulations return similar results.

Super-Kamiokande-I	Data	Total MC NEUT	Signal MC NEUT	Total MC NUANCE	Signal MC NUANCE
FC, FV, single-ring, spallation removed	8946 (100%)	8138.1(100%)	45.1 (100%)	8031.5 (100%)	41.2 (100%)
Sparse ring removal cut	8509 (95.1%)	7729.7 (95.0%)	31.7 (70.4%)	7673.4(95.5%)	29.3 (71.1%)
$E_{\rm vis} < 200$ MeV	2101 (23.5%)	1894.2 (23.3%)	29.7 (65.9%)	1843.5 (23.0%)	27.9 (67.7%)
Cone opening angle $<37°$	1161 (13.0%)	1020.0 (12.5%)	28.9 (64.2%)	1009.4(12.6%)	26.6 (64.5%)
Pattern ID estimator cut	74 (0.83%)	68.8 (0.85%)	25.6 (56.8%)	65.8 (0.82%)	22.7 (55.0%)

TABLE II. Summary of SK-II NC elastic selection. In this table the Monte-Carlo has been reweighted according to live time, solar activity for SK-II, as well as neutrino oscillations assuming $\Delta m^2 = 2.5 \times 10^{-3}$ eV^2 and $\sin^2 2\theta = 1$. The cut on the cone opening angle is tighter than in SK-I, since the fitter relies on a different ring edge finding method. Both NEUT and NUANCE simulations yield similar results.

Super-Kamiokande-II	Data	Total MC NEUT	Signal MC NEUT	Total MC NUANCE	Signal MC NUANCE
FC, FV, single-ring, spallation removed	4700 (100%)	4190.1 (100%)	18.9 (100%)	4174.2 (100%)	17.9 (100%)
Sparse ring removal cut	4464 (95.0%)	4004.6 (95.6%)	13.9 (73.3%)	3992.0(95.6%)	12.6 (70.4%)
$E_{\rm vis} < 200$ MeV	1169 (24.9%)	969.4 (23.3%)	12.8 (67.5%)	953.0 (22.8%)	11.8 (66.1%)
Cone opening angle $<35°$	261 (5.55%)	217.1 (5.18%)	11.6 (61.1%)	216.7 (5.2%)	10.6 (59.5%)
Pattern ID estimator cut	37 (0.79%)	39.9 (0.95%)	10.4 (54.9%)	39.6 (0.95%)	9.7 (54.5%)

is required to be positive. This selects events with a protonlike pattern.

The distribution of the variables is shown in Fig. 8. The efficiencies of all cuts are summarized in Tables I and II. In these tables, events labeled as signal are events with a single visible track caused by a proton above Cherenkov threshold; this is comprised of ~55% NC elastic events on protons, the rest being mostly neutral current pion production collisions where the pion was absorbed. These interactions are an irreducible background to a search for proton NC elastic events, but we include them in the signal since this analysis technique is designed to maximize the efficiency of proton track selection while reducing contamination from muon and pion tracks. At this stage, there are ~25.6 (~ 10.4) expected signal events in SK-I (SK-II).

B. Neural network selection

At this stage, the signal-to-noise ratio has been decreased from ~1/200 to ~1/3. It is possible to improve this using multivariate analysis techniques. Here we chose to use a neural network. We used the TMVA library [14] for this calculation.

TABLE III. Summary of neural network selection.

Run period	Data	Expected signal	Expected background
SK-I	27	22.1	12.2
SK-II	11	8.5	6.8

1. Neural network input variables and training

As inputs to the network, seven variables were used: the Cherenkov opening angle, the μ-like momentum of the event, the fitted protonlike length, the fitted protonlike momentum, the pattern likelihood difference, the number of decay electrons in the event, and the *normalized length*. The normalized proton length L_n is defined by

$$L_n = \frac{L}{L_{\rm max}(P)},$$

where L and P are the measured protonlike track length and momentum, and $L_{\rm max}(P)$ is the maximum path length in water for a proton of momentum P. Figure 9 shows the distributions of these variables for data and Monte-Carlo. Signal events are shown as hatched histograms.

A large sample of NC elastic events on protons was prepared to be used as signal for training purposes. Several samples of low momentum monochromatic charged pions (from 180 to 1000 MeV/c) and muons (from 140 to 500 MeV/c) were used as background training samples. All reconstruction algorithms and previous selection cuts were applied to those events, which were then fed into the neural network for training. Checks were conducted to make sure no overtraining occurred. The best architecture was found to be a single hidden layer with 6 neurons.

Since the distributions of the discriminating variables are different for SK-I and SK-II, two separate networks with identical architectures were used.

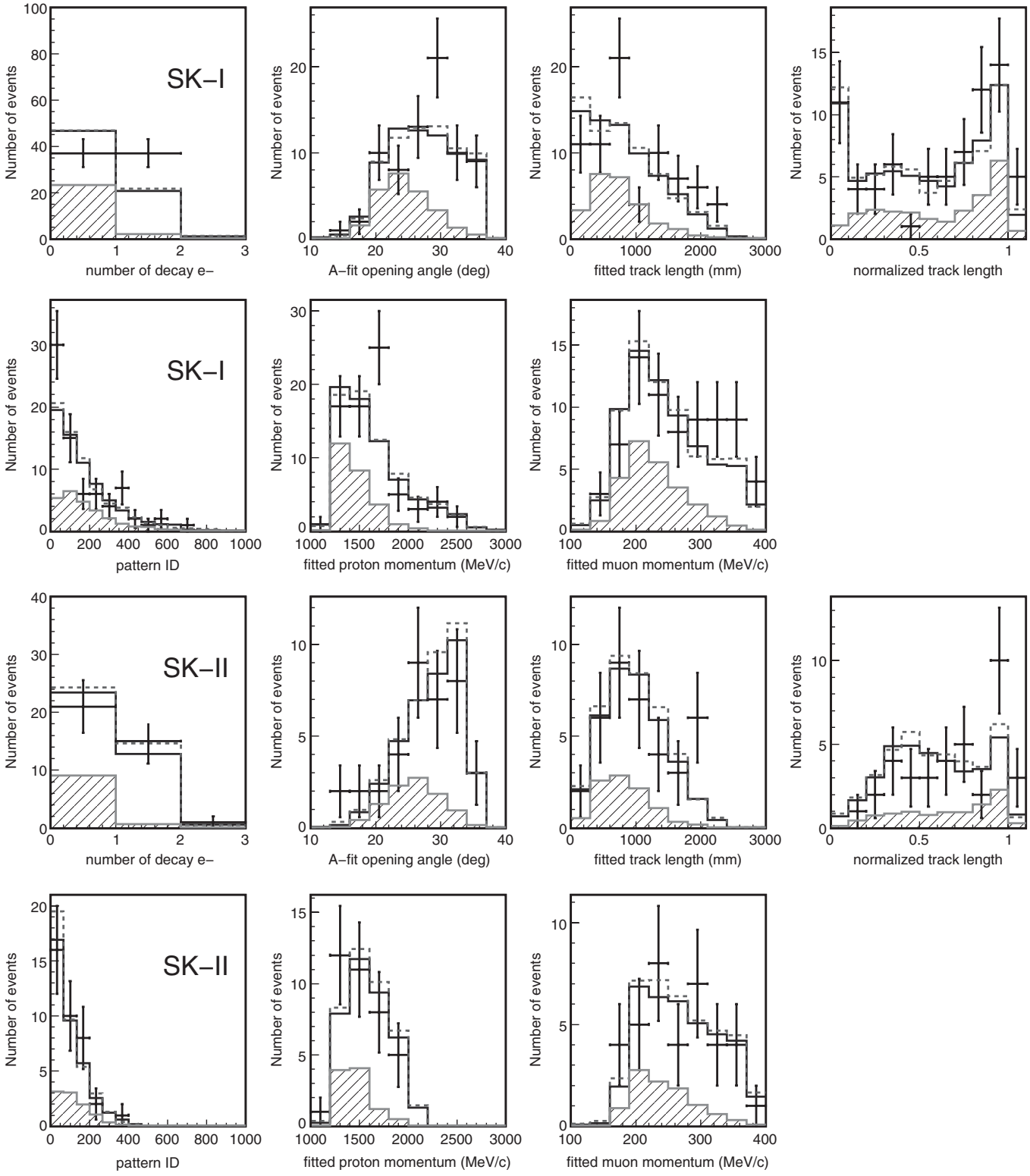

FIG. 9. Discriminating variables used as input for the neural network. The expectations from NEUT (solid line) and NUANCE (dashed line) are shown. The hatched histogram shows the fraction of signal events according to NEUT.

2. Neural network response

Figure 10 shows the response of the neural networks, labeled NN in what follows. Using the Monte-Carlo, we have studied the composition of the signal and background as a function of neural network response NN. Figure 11 shows the results. It should be noted that the neutral current content of the sample before any NN cut is 66%

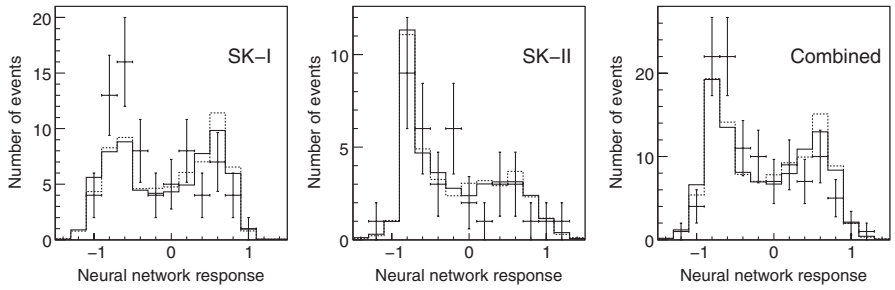

FIG. 10. Neural network response for data and MC (solid line: NEUT, dashed line: NUANCE). Left: SK-I, middle: SK-II, right: combined. The MC were oscillated with ($\Delta m^2 = 2.5 \times 10^{-3}$ eV^2, $\sin^2 2\theta = 1.0$).

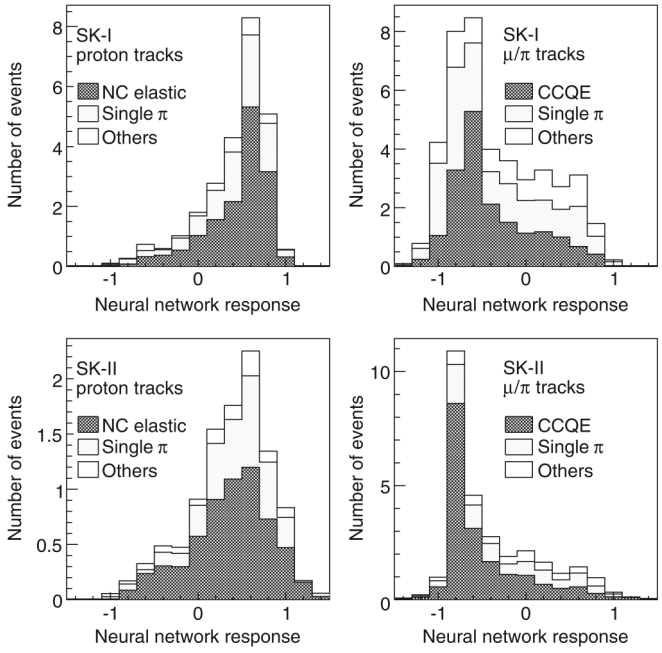

FIG. 11. Top: SK-I neural network response for signal and background, separated according to the main interaction modes. For signal events, the main mode is NC elastic on proton, followed by NC single-pion production where the pion is absorbed. The rest is mostly NC elastic on neutrons where the neutron produced a proton. Background mostly comes from low energy CCQE muon events, and pion tracks from single-pion interactions.

(45%) for SK-I (SK-II); when keeping only events with $NN > 0$, this fraction reaches 85% (76%). The $NN > 0$ cut was chosen because it maximizes the significance signal/$\sqrt{\text{signal} + \text{background}}$.

C. Results from the high purity neutral current proton enriched sample

After the $NN > 0$ cut we expect 34.3 events in SK-I data and 15.3 in SK-II data (see Table III); out of those, 22.1 and 8.5, respectively, are events with a single track caused by a visible proton; 13.1 and 5.0 (respectively) are neutral current elastic collisions on protons according to the NEUT simulation. We observe 27 events in SK-I and 11 events in SK-II.

We calculated the χ^2 of the data neural output distributions to Monte-Carlo with and without single visible proton events (using 6 bins from -1 to 1 to increase the bin contents for statistical purposes). Using the Monte-Carlo including all event, the χ^2 is 9.3 for 6 bins (probability 15.7%); when all visible protons are excluded the χ^2 value is 15.8 (probability 1.5%). The data are clearly compatible with the observation of single visible protons.

We have determined that in this final sample the proton-like particle has a mean angle of 38° (41° for SK-II) with the incoming neutrino track, which means that the proton still has some correlation with the original neutrino direction and allows zenith angle studies. In order to cancel out any flux normalization uncertainties we calculate the up-down asymmetry $\frac{U-D}{U+D}$ where up-going events are those with $-\cos\theta_{\text{zenith}} < -0.2$ and down-going events have $-\cos\theta_{\text{zenith}} > 0.2$. The results are summarized in Table IV and Fig. 12, and are compatible with no sterile oscillations. Clearly the statistics of our sample are too weak to extract meaningful information on $\nu_\mu \rightarrow \nu_{\text{sterile}}$ oscillation. Full $\nu_\mu \rightarrow \nu_{\text{sterile}}$ oscillations (already ruled out

TABLE IV. Up- and down-going events with corresponding asymmetries. All NC elastic selection cuts have been applied, including the $NN > 0$ cut. In this table the Monte-Carlo has been reweighted according to livetime, solar wind activity for SK-II, as well as neutrino oscillations assuming $\Delta m^2 = 2.5 \times 10^{-3}$ eV^2 and $\sin^2 2\theta = 1$. The error bars for simulated events correspond to Monte-Carlo statistics.

	Up	Down	$\frac{U-D}{U+D} \pm$ stat
SK-I data	11	11	0 ± 0.21
SK-I NEUT MC	13.76	14.44	-0.024 ± 0.026
SK-I NUANCE MC	12.61	11.82	0.032 ± 0.038
SK-II data	2	5	-0.43 ± 0.34
SK-II NEUT MC	5.88	6.38	-0.041 ± 0.033
SK-II NUANCE MC	5.44	6.23	-0.068 ± 0.040
Combined data	13	16	-0.10 ± 0.19
Combined NEUT MC	19.63	20.81	-0.029 ± 0.021
Combined NUANCE MC	18.05	18.05	0.00 ± 0.029

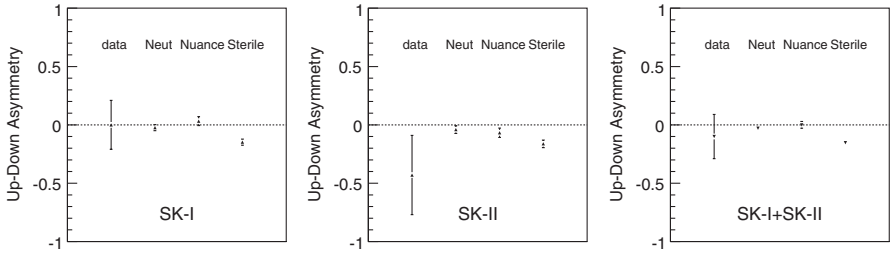

FIG. 12. Up-down asymmetries with statistical errors. In each plot the present measurement is the left-most point, labeled "data." The middle points labeled NEUT and NUANCE show the MC expectation including 2-flavor $\nu_\mu \rightarrow \nu_\tau$ oscillation, with MC statistical error only. The right-most point labeled "sterile" shows the expectation of the NEUT MC assuming oscillations are only $\nu_\mu \rightarrow \nu_{\text{sterile}}$. The error bars for simulated events correspond to Monte-Carlo statistics.

by [15]) would result in an asymmetry of $\approx -15\%$ which is comparable with our data's present statistical error. Super-Kamiokande has also already constrained the admixture of sterile neutrinos to be less than 26% at 90% C.L. [16] using the so-called 2 + 2 model parametrized in [17]. The amount of sterile admixture is not measurable with the single visible proton sample alone. Although such a study is beyond the scope of this paper, the single visible proton sample could be merged with other samples sensitive to sterile neutrinos and included in a larger fit.

V. SEARCH FOR CHARGED-CURRENT QUASIELASTIC EVENTS

Another study made possible with proton identification is the search for charged-current quasielastic (CCQE) events with both the lepton and the proton above Cherenkov threshold. The reaction is $\nu + n \rightarrow p +$ lepton. Having a proton in the final state can only happen for neutrinos and not antineutrinos, providing a possibility for neutrino tagging, which has so far not been done in Super-Kamiokande. Knowledge of both outgoing tracks allows kinematic reconstruction of the incoming atmospheric neutrino, which has never been reported in a large water Cherenkov detector: in the zenith-angle Super-Kamiokande analyses with atmospheric fully-contained data [2], the lepton direction in the data and Monte-Carlo are compared directly. From our Monte-Carlo simulations, we expect about 150 (75) events in the SK-I (SK-II) data sample with both tracks above Cherenkov threshold, assuming 2-flavor oscillations with ($\Delta m^2 = 2.5 \times 10^{-3}$ eV^2, $\sin^2 2\theta = 1$).

We have focused on events with either one or two rings reconstructed by the standard ring finder. Each class requires a different analysis technique and will be studied separately. Figure 13 shows two typical CCQE events, one for each class.

A. Events with two fitted rings

The first case to consider is that for which both rings were identified by the standard ring finder described earlier. When this happens, in more than 97% of the cases the proton is found as the second ring, so we make that assumption in this analysis. The vertex, ring directions, and lepton momentum are known from the reconstruction algorithms. We have modified the light pattern engine to superimpose a lepton and a proton pattern; the lepton ring is kept fixed, its parameters being set to the fitted informa-

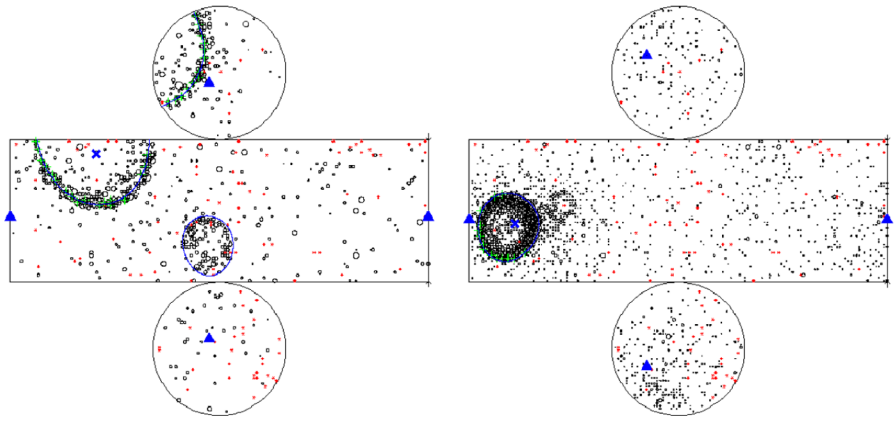

FIG. 13 (color online). Event displays of Monte-Carlo CCQE events, where both the muon (large ring) and the proton (smaller ring) are visible. In the left figure, both tracks were found by the standard fitter (the thin lines show the fit results). In the figure on the right only the lepton (a muon in this example) was fitted; the proton is visible as a smaller ring next to the muon.

tion. The likelihood of this combined pattern is then maximized using the same MINUIT-based fitting, varying the proton momentum and track length. The normalization of the light patterns is done using the same procedure as for single-ring protons, simply adding the lepton pattern to it.

Then, a second likelihood corresponding to a lepton and a muon light pattern is calculated. The discriminating variables are the fitted protonlike momentum and track length, as well as the log-likelihood difference $\log L_{\text{lepton+proton}} - \log L_{\text{lepton+muon}}$.

CCQE selection relies on the following cuts:

(1) We first select only vertices inside the fiducial volume, with two fully-contained rings, and $100 < E_{\text{vis}} < 4000$ MeV (note that for the CCQE search the energies are high enough that no spallation cut is necessary).

(2) Our next cut aims at removing background coming from pion production, where the second ring was in fact caused by a charged pion. In this case, the fitted protonlike momentum of the track is typically about 1.6 GeV/c, because the charged pions have typical momenta between 200 and 300 MeV, and thus a ring opening angle of roughly 30°. However, the fitted path length is very short (about 20 cm) because of pion interactions. In order to remove the charged pions, a linear cut on the protonlike momentum and track lengths $A < P < B \times L(\text{m}) + C$, with $A = C = 1.1$ GeV/c and $B = 7/6$ GeV/c/m. This selection can be seen in Fig. 14.

(3) We then require that the opening angle of the second ring be less than 34°, to select particles with low β.

(4) To select proton tracks a cut on the pattern likelihood difference $\log(L_{\text{lepton+proton}}) - \log(L_{\text{lepton+muon}}) > 0$ is applied.

(5) At this stage the sample still contains non-CCQE events, mostly corresponding to misidentified pions. To improve CCQE selection we use event kinematics. Let V be the 4-vector

$$V = P_p + P_l - P_n,$$

where P_p, P_l, and P_n are the 4-momenta of the proton, lepton, and target neutron. For a true CCQE event, V must be equal to P_ν, the neutrino 4-momentum, and consequently the Lorentz invariant quantity V^2 must be $m_\nu^2 \approx 0$ eV^2/c^4. On the other hand, for a non-CCQE event, V is not equal to the neutrino 4-momentum and its square will be nonzero. In practice, nuclear effects, such as Fermi motion of the neutron or scattering of the outgoing nucleon, and detector effects will smear the resolution on V^2, but it is still a powerful tool, as can be seen in Figs. 14 and 15, with CCQE events peaked around 0. We apply a cut $-0.75 < V^2 < 1.5$ GeV/c^2 for two-ring events.

Figures 14 and 15 show the distributions of these variables for data and Monte-Carlo for SK-I and SK-II, showing good agreement. The results are shown in Tables V and VI. The overall signal efficiency is 42–45%, with an expected signal-to-background ratio of 1.4 to 1. The high signal efficiency can be explained by the fact that those protons have high enough momenta to have been found by the ring fitter, and are well above Cherenkov threshold.

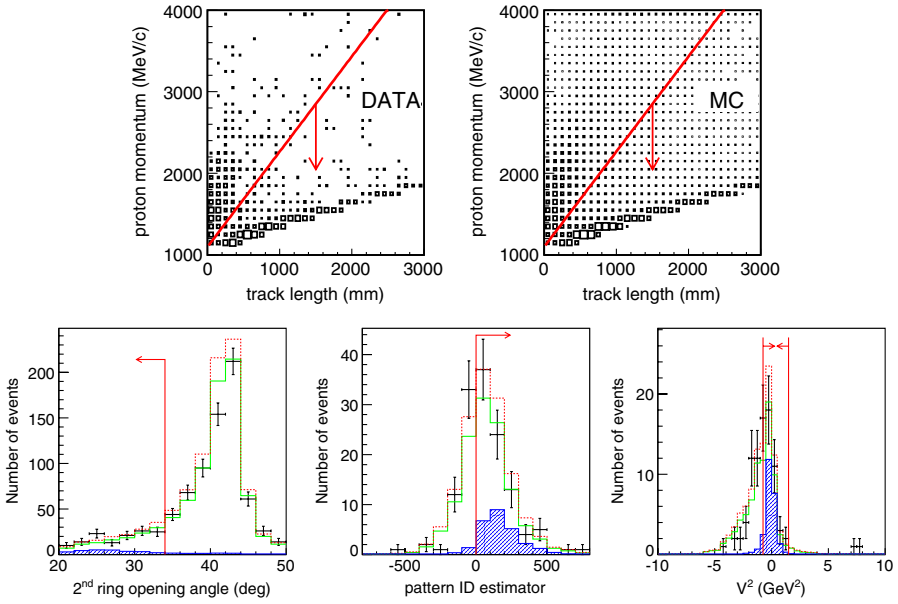

FIG. 14 (color online). Distribution of analysis variables with cuts for two-ring CCQE event selection in SK-I. The top two plots are two-dimensional L, P distributions for data and MC, shown with the charged pion removal cut; the arrows show the selected domain. In the bottom three plots, the solid and dashed lines show Monte-Carlo expectation from NEUT and NUANCE, with oscillation reweighting, but no correction for the absolute flux normalization. The hatched regions show the contribution from CCQE events.

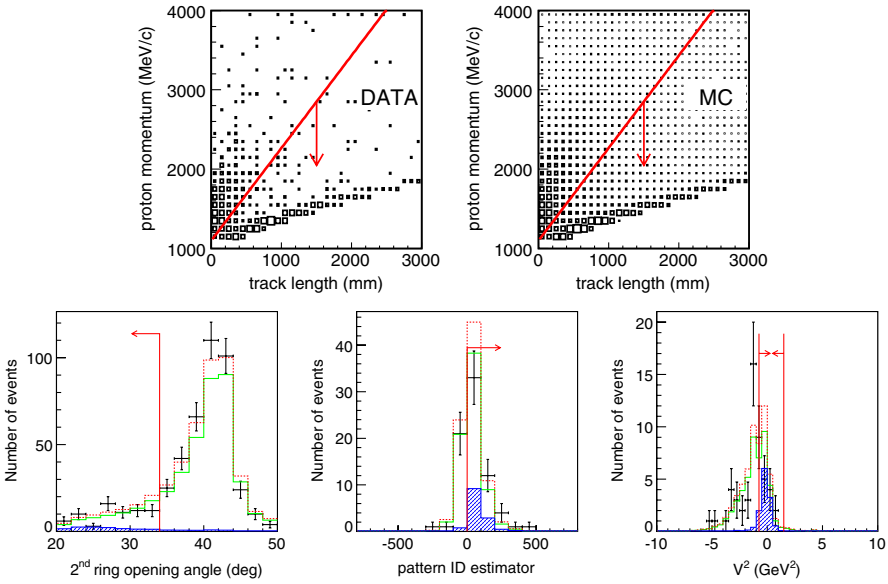

FIG. 15 (color online). Distribution of analysis variables with cuts for two-ring CCQE event selection in SK-II. The top two plots are two-dimensional L, P distributions for data and MC, shown with the charged pion removal cut; the arrows show the selected domain. In the bottom three plots, the solid and dashed lines show Monte-Carlo expectation from NEUT and NUANCE, with oscillation reweighting, but no correction for the absolute flux normalization. The hatched region shows the contribution from CCQE events.

Monte-Carlo studies of the selected events show that of the 38 (19) events in the final SK-I (SK-II) sample, 33 (16) do have their second ring caused by a proton (the rest mostly come from gammas and charged pions), and 22 (11) of those are CCQE signal events. The non-CCQE proton rings mostly come from CC pion events, and are an irreducible background to the CCQE search. It is worth noting that at this stage the sample contains 93% neutrinos and 7% antineutrinos.

B. Events with a single fitted ring after standard algorithms

Monte-Carlo studies show that there are potentially ≈ 150 CCQE events in the SK-I and SK-II data sets with a proton above threshold where the proton was missed by the standard ring finder. Such events only have a single fitted ring corresponding to the brighter lepton track. The proton ring is weak, but visible by eye-scan. A dedicated ring finding algorithm to select these weak rings was developed. The vertex and lepton track are very well

TABLE V. Summary of SK-I CCQE selection for two-ring events. In this table the Monte-Carlo has been reweighted according to livetime, solar wind activity for SK-I, as well as neutrino oscillations assuming $\Delta m^2 = 2.5 \times 10^{-3}$ eV^2 and $\sin^2 2\theta = 1$.

SK-I	Data	Total MC	Signal MC
FC, FV, two-ring, $0.1 < E_{vis} < 4$ GeV	1876 (100%)	1773 (100%)	50.12 (100%)
$1.1 < P < 7/6L(m) + 1.1$ GeV/c	829 (44.19%)	839.4(47.34%)	36.12(72.1%)
Angle of second cone $<34°$	135 (7.2%)	124.1(7.0%)	27.2 (54.3%)
Pattern ID cut	86 (4.58%)	82.88 (4.67%)	25.26 (50.4%)
$-0.75 < V^2 < 1.5$ GeV^2	44 (2.35%)	38.59 (2.18%)	22.71 (45.31%)

TABLE VI. Summary of SK-II CCQE selection for two-ring events. In this table the Monte-Carlo has been reweighted according to livetime, solar activity for SK-II, as well as neutrino oscillations assuming $\Delta m^2 = 2.5 \times 10^{-3}$ eV^2 and $\sin^2 2\theta = 1$.

SK-II	Data	Total MC	Signal MC
FC, FV, two-ring, $0.1 < E_{vis} < 4$ GeV	1023 (100%)	910.8(100%)	26.2 (100%)
$1.1 < P < 7/6L(m) + 1.1$ GeV/c	471 (46.04%)	417.1(45.79%)	18.3(68.8%)
Angle of second cone $<34°$	74 (7.23%)	72.73(7.99%)	13.7(52.3%)
Pattern ID cut	51 (4.99%)	49.64 (5.5%)	12.84 (49.01%)
$-0.75 < V^2 < 1.5$ GeV^2	12 (1.17%)	18.99 (2.09%)	11.22 (42.81%)

known at this stage of the reconstruction: as single-ring events, the refined vertex fitter (see Sec. III B) was applied, and the e-like or μ-like nature of the track is known. The observed charge pattern is projected into a 50×50 grid in $(\cos\theta, \phi)$ spherical coordinates around the lepton track. The expected light from the lepton is subtracted, and the maximum amount of charge in a 25×10 sliding window is found, avoiding directions too close to the lepton track. The corresponding average direction is used as a starting position in a precise grid fit, where a ring-shaped pattern is fitted to the observed light pattern, varying the direction and opening angle until the best match is found. This direction fit yields a new ring candidate, which could be a proton or another particle, or just a region with higher charge in a bona fide single-ring event.

Therefore, we also calculate the distribution of charges $Q(\theta)$ as a function of opening angle θ from the candidate direction, subtracting the expected light contribution from the lepton. We then calculate the ratio of the integrated charge around the maximum of this distribution to an average of the charge at low and high values of θ. This estimator Q_{dens}, should be large for a true Cherenkov ring, since a real ring should have a marked peak in $Q(\theta)$ near the Cherenkov edge. A similar technique is also used in standard ring counting to reject fake seeds found by the Hough transform.

Using the lepton's fitted information and the new fitted direction, we add a lepton and a proton's expected charge patterns. The likelihood of this combined pattern is maximized as already outlined previously, yielding $\log(L_{\mathrm{lepton+proton}})$. Another pattern likelihood corresponding to the lepton alone $\log(L_{\mathrm{lepton\ alone}})$ is also calculated, and the pattern ID estimator

$$\Delta L = \log[\log(L_{\mathrm{lepton+proton}}) - \log(L_{\mathrm{lepton\ alone}})]$$

is constructed. A high value of this estimator corresponds to a protonlike track candidate.

Our analysis of single-ring events closely follows the steps outlined for the two-ring search.

(1) We select single-ring fully-contained events within the fiducial volume and $0.1 < \mathrm{E_{vis}} < 4$ GeV.
(2) Using the output of the proton pattern fitter on the new candidate ring, we apply the cuts $A < P < B \times L(\mathrm{m}) + C$, with $A = C = 1.1$ GeV/c and $B = 7/6$ GeV/c/m. We also require that $L < 2$ m. These cuts aim at rejecting rings coming from pions as in Sec. V A, as well as fake rings which are usually fitted with a very low P and L.
(3) We then require $\log Q_{\mathrm{dens}} > 0$, to remove bad ring candidates.
(4) In order to improve proton selection we then apply the cut $\Delta L > 3$, where ΔL is the pattern ID estimator defined above.
(5) Finally to reject non-CCQE background as well as other nonproton rings we ask that $V^2 > -0.75$ GeV/c^2, using the same definition of V as in the previous section.

The final signal efficiency is about 21% (18% in SK-II), for the cases where the proton ring is potentially visible. This is lower than in the two-ring case because for single-ring events, most of those protons are just above Cherenkov threshold and therefore very hard to find. Signal-to-noise after all cuts is about 1.1 to 1. We expect to recover 20 (9) CCQE events in SK-I (SK-II), almost doubling our statistics. The efficiencies are summarized in Tables VII and VIII, and the distributions of the variables are shown in Figs. 16 and 17.

TABLE VII. Summary of SK-I CCQE selection for single-ring events. In this table the Monte-Carlo has been reweighted according to livetime, solar activity for SK-I, as well as neutrino oscillations assuming $\Delta m^2 = 2.5 \times 10^{-3}$ eV^2 and $\sin^2 2\theta = 1$.

SK-I	Data	Total MC	Signal MC
FC, FV, single-ring, $0.1 < \mathrm{E_{vis}} < 4$ GeV	7224 (100%)	6523 (100%)	94.4 (100%)
$1.1 < P < 7/6L(m) + 1.1$ and $L < 2$ m	1456 (20.2%)	1488 (22.8%)	44.8 (47.5%)
Q density cut	235 (3.25%)	213.1 (3.3%)	22.95 (24.32%)
Pattern ID cut	76 (1.05%)	66.01 (1.01%)	21.04 (22.29%)
$V^2 > -0.75$ GeV^2	47 (0.65%)	38.69 (0.59%)	20.33 (21.53%)

TABLE VIII. Summary of SK-II CCQE selection for single-ring events. In this table the Monte-Carlo has been reweighted according to livetime, solar activity for SK-II, as well as neutrino oscillations assuming $\Delta m^2 = 2.5 \times 10^{-3}$eV^2 and $\sin^2 2\theta = 1$.

SK-II	Data	Total MC	Signal MC
FC, FV, single-ring, $0.1 < \mathrm{E_{vis}} < 4$ GeV	3874 (100%)	3463 (100%)	50.71 (100%)
$1.1 < P < 7/6L(m) + 1.1$ and $L < 2$ m	702 (18.12%)	625.2 (18.1%)	20.45 (40.3%)
Q density cut	193 (4.98%)	175.2 (5.1%)	12.75 (25.14%)
Pattern ID cut	29 (0.75%)	27.53(0.80%)	9.58 (18.9%)
$V^2 > -0.75$ GeV^2	22 (0.57%)	17.6 (0.51%)	9.2 (18.1%)

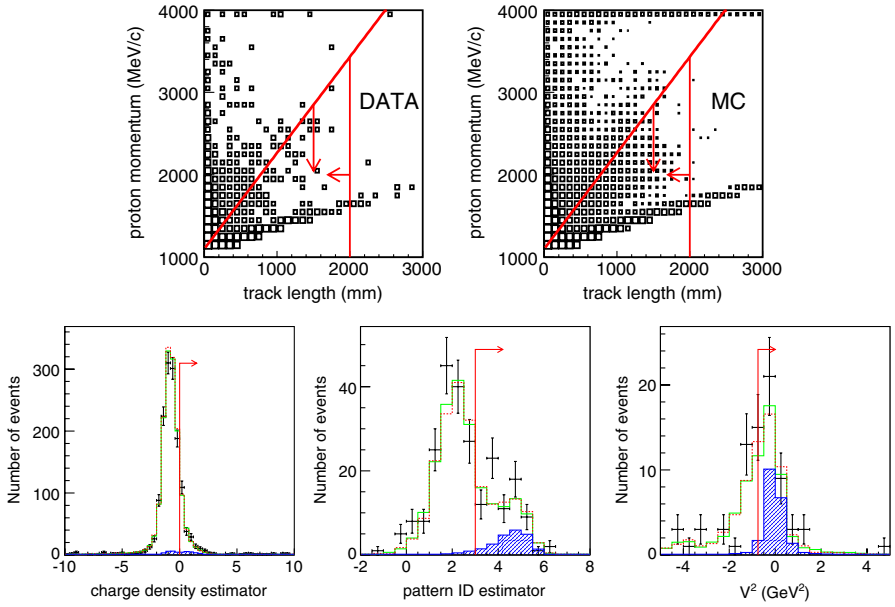

FIG. 16 (color online). Distribution of analysis variables with cuts for single-ring CCQE event selection in SK-I. The top two plots are two-dimensional L, P distributions for data and MC, shown with the charged pion removal cut; the arrow shows the selected domain. In the bottom three plots, the solid and dashed lines show Monte-Carlo expectation from NEUT and NUANCE, with oscillation reweighting, but no correction for the absolute flux normalization. The hatched region shows the contribution from CCQE events.

In the final sample in SK-I (SK-II), 31 (13) events out of the final 39 (18) do have a proton track missed by the ring finder that was recovered by this new fitter; 11 (4) of those are non-CCQE interactions with a visible protons (mostly CC pion production) and are an irreducible background to the CCQE sample. After all cuts the single-ring sample contains 90% neutrinos and 10% antineutrinos.

C. Kinematic reconstruction of atmospheric neutrinos

Once we have a CCQE enriched sample, kinematic reconstruction of the incoming neutrino is straightforward, assuming that the target neutron is immobile. Writing the total momentum as P_{tot} and the direction as $\mathbf{d}$ the following equations hold:

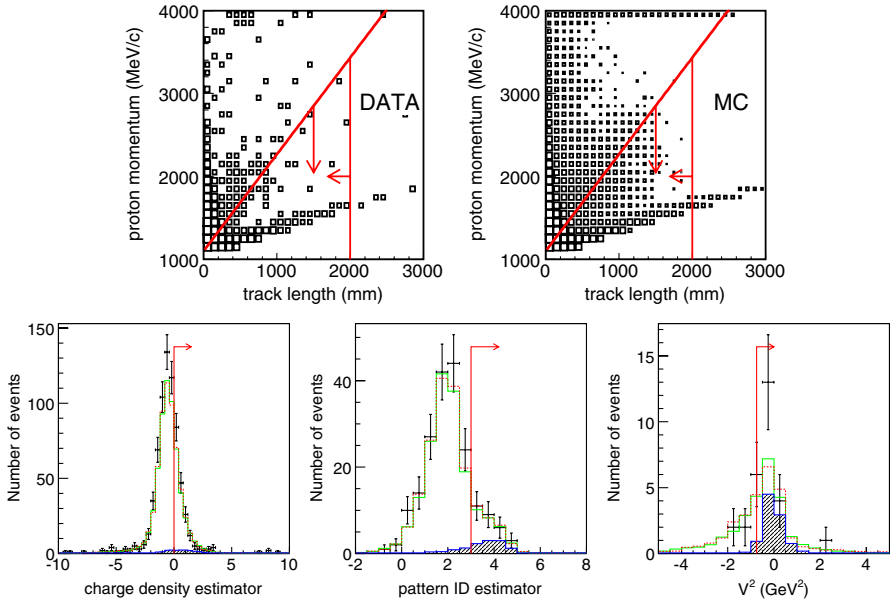

FIG. 17 (color online). Distribution of analysis variables with cuts for single-ring CCQE events selection in SK-II. The top two plots are two-dimensional L, P distributions for data and MC, shown with the charged pion removal cut; the arrow shows the selected domain. In the bottom three plots, the solid and dashed lines show Monte-Carlo expectation from NEUT and NUANCE, with oscillation reweighting, but no correction for the absolute flux normalization. The hatched region shows the contribution from CCQE events.

TABLE IX. Energy and angular resolution of the kinematic reconstruction shown in the text. Since the energy resolution distributions are asymmetric we report 68.3% centered confidence intervals.

		Two-ring events		Single-ring events	
		CCQE	TOTAL	CCQE	TOTAL
SK-I	Angular resolution (°)	8.0°	12.3°	8.1°	14.9°
	Energy resolution (%)	$^{+10.7}_{-4.4}$	$^{+10.6}_{-17.2}$	$^{+9.9}_{-6.2}$	$^{+13.6}_{-16.7}$
SK-II	Angular resolution (°)	8.6°	12.0°	8.1°	16.2°
	Energy resolution (%)	$^{+10.3}_{-5.9}$	$^{+10.8}_{-17.9}$	$^{+9.6}_{-5.8}$	$^{+10.8}_{-22.0}$

$$P_{\text{tot}} = \sqrt{(\mathbf{P}_{\text{p}} + \mathbf{P}_{\text{l}})^2},$$

and

$$\mathbf{d} = \frac{1}{P_{\text{tot}}}(\mathbf{P}_{\text{p}} + \mathbf{P}_{\text{l}}),$$

where $\mathbf{P}_{\text{p}}$ and $\mathbf{P}_{\text{l}}$ are the proton and lepton 3-momenta. Since we assume that all selected events are CCQE we use $E = P_{\text{tot}}$ for the neutrino energy. Using simulated data we have checked the angular resolution on neutrino track direction, as well as the energy resolution. The energy reconstruction process has a tail toward negative values for non-CCQE events reconstructed with this technique and is non-Gaussian. We have computed a 68.3% confidence interval centered on the peak of the distribution. The angular and energy resolutions are summarized in Table IX.

1. Zenith angle distributions

To examine the evidence of zenith angle distortion in the enhanced CCQE sample, we first separate it into electron and muon neutrino interactions. Each event is categorized according to the lepton's e-like or μ-like identification. After this characterization, we kinematically reconstruct each event. The reconstructed neutrino energy spectra are shown in Fig. 18.

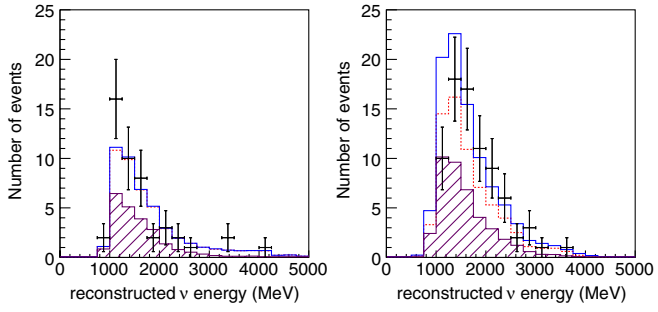

FIG. 18 (color online). Reconstructed energy spectra of the CCQE enriched sample, e-like events are on the left and μ-like events on the right. The hatched region shows the CCQE fraction from NEUT. The solid histograms correspond to our nonoscillated Monte-Carlo simulation, while the dashed histograms show the prediction with oscillations assuming $\Delta m^2 = 2.5 \times 10^{-3}$ eV^2 and $\sin^2 2\theta = 1$.

Figure 19 shows the reconstructed neutrino zenith angle distribution, along with the MC expectation with and without oscillations. Clearly, the distributions are consistent with our measurement of oscillation parameters presented in [2].

For the events selected in this analysis, which are mostly in the sub-GeV region, the lepton angular correlation to the incoming neutrino is weak ($\sim 80°$ resolution). However, with neutrino kinematic reconstruction, the angular resolution on the neutrino track reaches 12° for ν_μ and 16° for ν_e, making the expected zenith angle distortion in the neutrino direction of μ-like sample clearly visible. The observed up-down asymmetry using neutrino track reconstruction is -0.52 ± 0.17(stat) for μ-like events and -0.06 ± 0.24 for e-like events, compatible with $\nu_\mu \rightarrow \nu_\tau$ neutrino oscillations. For comparison purposes the asymmetries obtained using the lepton zenith angle are -0.059 ± 0.24 for μ-like and 0 ± 0.22 for e-like events.

The distributions in Fig. 19 can be contrasted with those in Fig. 20. In the second set of figures, the lepton direction rather than the kinematically reconstructed neutrino direction is shown for the CCQE enhanced sample. As can be seen, there is little sign of the oscillation distortion in the lepton zenith angle distributions. The correlation between the incoming neutrino and outgoing lepton direction has been lost. Most of the events in the CCQE enriched sample have a large angle between the neutrino and lepton by virtue of the fact that a large momentum was given to the

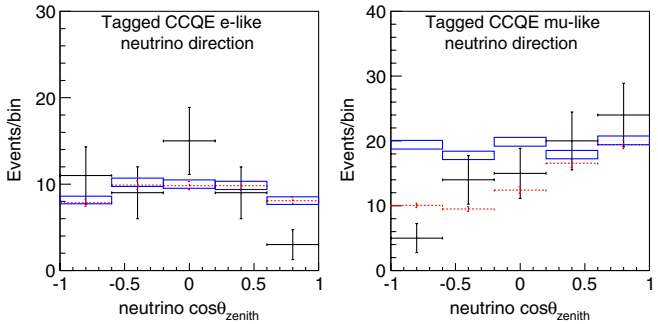

FIG. 19 (color online). Reconstructed neutrino zenith angle of the CCQE enriched sample, e-like events are on the left and μ-like events on the right. The box histograms correspond to our nonoscillated Monte-Carlo simulation, while the dashed histograms show the prediction with oscillations assuming $\Delta m^2 = 2.5 \times 10^{-3}$ eV^2 and $\sin^2 2\theta = 1$.

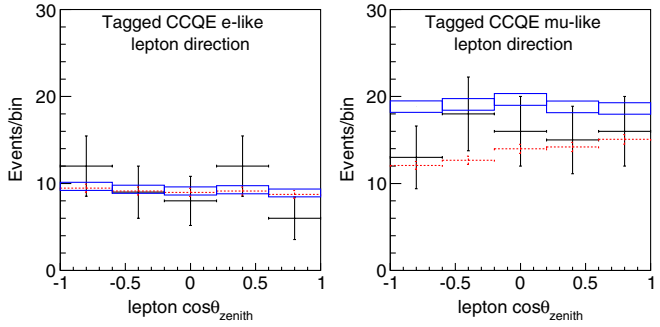

FIG. 20 (color online). The lepton zenith angle of the CCQE enriched sample, e-like events are on the left and μ-like events on the right. The box histograms correspond to our nonoscillated Monte-Carlo simulation, while the dashed histograms show the prediction with oscillations assuming $\Delta m^2 = 2.5 \times 10^{-3}$ eV^2 and $\sin^2 2\theta = 1$.

proton in the reaction, resulting in the proton being visible and the lepton having a large transverse momentum to balance it.

Approximately one half of the sample is made up of two-ring events where one of the rings has been identified as a proton. In order to obtain a high charged-current purity, in [2] only multiring events with a leading muon (not an electron) were included. For the same reason, a minimum requirement of 600 MeV/c was imposed on the leading muon momentum for the sub-GeV multiring muons. Both of those restrictions have been lifted here. In the analysis of [2], even applying the extra requirements used in the μ-like multiring sample resulted in a CC purity of 54% in the e-like multiring sample. The use of the proton tag in the CCQE enhanced sample results in charged-current purity of 88% for e-like events and 95% for μ-like events.

In the combined single-ring and two-ring enriched CCQE sample the zenith distortion is clearly seen. Additionally, although the statistics are too low to be usable (there are only about 20 events in total), according to Monte Carlo, the data are expected to show a zenith angle suppression even for events with the momentum of the lepton less than 400 MeV. As shown in [2], in previous analyses, using the lepton direction for these events resulted in the complete loss of the initial neutrino direction.

The use of the CCQE sample restores zenith angle pointing to a low energy portion of the atmospheric sample which previously had no observed zenith angle distortion, and adds events to the sample with good pointing which were not previously considered. This is an important further cross-check of the both the analysis technique and the oscillation hypothesis.

2. L/E distributions

The neutrino path length L is a simple function of the zenith angle however, there are two main sources of uncertainty:

(i) Near the horizon, a small error on the zenith angle leads to a large error in L since $dL/d\cos\theta_{\rm zenith}$ is large.

(ii) There is an additional uncertainty in the production height of atmospheric neutrinos. While it is negligible compared to the overall travel length for neutrino produced on the far side of the Earth, it is comparable to the total L for neutrinos produced directly above Super-Kamiokande. The model from Honda *et al.*[9] is used to estimate the production height. For a given zenith angle, L is the average path length over 20 samplings from the production height distribution.

In this analysis, we use the reconstructed neutrino zenith angle to estimate L; E is the kinematically reconstructed ν energy defined in Sec. V C. This has not been attempted so far in Super-Kamiokande; the method reported in [18] used an energy estimator based on the total energy of all charged particles in the ID, and the neutrino zenith angle was obtained using the lepton zenith angle. Figure 21 is the distribution of L/E for events with a primary μ-like ring in the CCQE sample. SK-I and SK-II and single- and two-ring samples were combined together to increase statistics. The agreement with the oscillated distribution is very good.

These distributions can be used in $\nu_\mu \rightarrow \nu_\tau$ oscillation searches. Binning the e-like and μ-like data and MC $\log_{10}(L/E)$ distributions (5 equally spaced bins from 0 to 5 for both samples), we use the following Poisson likelihood ratio [19]:

$$\chi^2 = \sum_{i=2}^{5}\left((M_{\rm MC} - N_{\rm DATA}) + N_{\rm DATA}\log\frac{N_{\rm DATA}}{N_{\rm MC}}\right) + \sum_{j=2}^{6}\varepsilon_j^2/\sigma_j^2.$$

σ_j is the estimated uncertainty on each ε_j parameter; these variables describe the sources of systematic errors and are

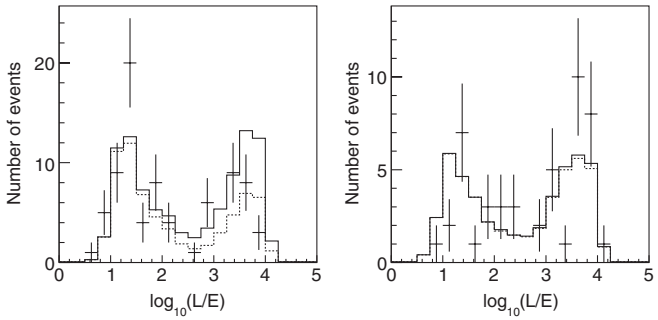

FIG. 21. Distribution of L/E for the combined CCQE enriched μ-like (left) and e-like (right) samples. The continuous lines show the expectation from NEUT without ν oscillations, while the dashed lines show the expectation with $\nu_\mu \rightarrow \nu_\tau$ oscillations with $\Delta m^2 = 2.5 \times 10^{-3}$ eV^2 and $\sin^2 2\theta = 1$.

adjusted during the fit. N_{MC} is the weighted sum of Monte-Carlo events, taking into account livetime and solar activity. Oscillation probabilities and systematic errors are taken into account using a technique similar to that of [20]. The weight of each Monte-Carlo event is:

$$w = F(1+\varepsilon_1)(E_\nu/2\ \mathrm{GeV})^{\varepsilon_2} \times P(\sin^2 2\theta, \Delta m^2, (1+\varepsilon_3)L/E_\nu)(1\pm\varepsilon_4/2) \times (1\pm\varepsilon_5/2),$$

where F is a numerical factor accounting for livetime normalization and solar activity, E_ν is the true neutrino energy, L the neutrino path length, and the function P is the oscillation probability. For each event, 20 values of L are obtained by sampling the production height distribution; P is the arithmetic average of the oscillation probabilities obtained for each of these lengths. The ε_j parameters have the following meanings:

(i) ε_1 represents the uncertainty on the absolute normalization of the sample. This includes flux uncertainties (8% in this energy range [9]), and also the systematic uncertainty on our CCQE event selection, which we estimate to be 14.4% based on Monte-Carlo studies. Since the combined error is large, it is a free parameter in the fit.

(ii) ε_2 is the uncertainty on the neutrino flux spectral index, with $\sigma_2 = 0.05$ as in [20].

(iii) ε_3 is a systematic error on the Monte-Carlo L/E ratio, coming from uncertainties in the production height, and absolute neutrino energy scale. Following [2] its width is set to 10%.

(iv) ε_4 describes the systematic error on e/μ separation and uncertainties on the flavor content of the atmospheric flux: in the definition of w the sign is negative for μ-like and positive for e-like, leading to complete anticorrelation between the ν_μ and ν_e samples. Since SK-I and SK-II are combined, we have used a conservative estimate of 15% for this error.

(v) ε_5 accounts for the uncertainty in the non-CCQE background selection efficiency, as well as for the CCQE/non-CCQE cross-section ratio; the sign preceding ε_5 in the definition of w is positive for CCQE and negative for non-CCQE events. We have assumed this ratio to be known to 10% in our simulation.

(vi) Finally one last parameter ε_6 is used to shift the reconstructed value of $\log_{10}(L/E)$ to account for biases in the kinematic reconstruction technique. Combining energy and direction reconstruction errors, we conservatively estimate the width of this parameter to be 10%.

We have used a 201×201 grid in $\log_{10}\Delta m^2$ and $\sin^2 2\theta$; at each point on the grid the ε_j were fitted using MINUIT. The best fit point is found in the unphysical region at ($\Delta m^2 = 1.310^{-4}$ eV^2, $\sin^2 2\theta = 1.3$), with $\chi^2_{\mathrm{min}} = 6.70/8$ d.o.f. The best fit in the physical region occurs at ($\Delta m^2 = 3.410^{-4}$ eV^2, $\sin^2 2\theta = 1.0$) at $\chi^2_{\mathrm{min,phys}} = 7.98/8$ d.o.f. Figure 22 shows the 68.3%, 90%, and 99% allowed regions ; these contours are located at $\chi^2_{\mathrm{min,phys}} + 2.86$, 5.32, and 10.02, respectively, using the same method as in [2]. With the low statistics of this sample, the allowed region is large. They are consistent with our previous, more precise results: the best fit point reported in our previous publications is accepted at better than 1σ. The no-oscillation point is rejected at 3σ ($\chi^2_{\mathrm{noosc}} - \chi^2_{\mathrm{min,phys}} = 12.95$). The systematic parameters at the best fit are summarized in Table X. The kinematically reconstructed CCQE sample used here has roughly half the statistics of the Soudan-2 tracking calorimeter experiment for which a similar analysis was performed [21].

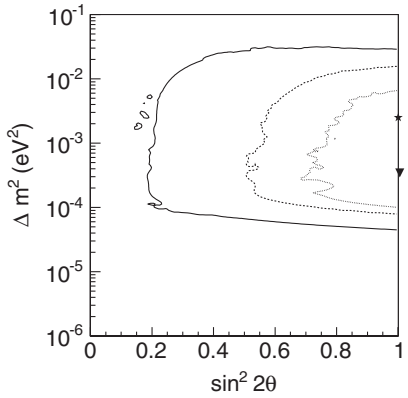

FIG. 22. Allowed regions at 68.3% (dotted line), 90% (dashed line) and 99% (solid line) C.L. for $\nu_\mu \rightarrow \nu_\tau$ oscillations from the CCQE kinematically reconstructed samples. The star shows the positions of the best fit from [2], while the triangle shows the position of the best fit for this sample in the physical region. These allowed regions are consistent with previously published results and exclude the no-oscillation hypothesis at greater than 3-sigma.

It must be noted that the CCQE selection method selects a quasipure sample of neutrinos ($\approx 90\%$). This could potentially have sensitivity to the mass hierarchy and other CP-odd effects.

TABLE X. Systematic parameters and their best fit values.

Parameter	Meaning	Uncertainty	Value at best fit
ε_1	absolute normalization	(free)	6.5%
ε_2	spectral index	0.05	−0.0006
ε_3	Error on true L/E	10%	−1.9%
ε_4	e/μ ratio	15%	−2.1%
ε_5	CCQE/non-CCQE ratio	10%	0.2%
ε_6	shift in reconstructed L/E	10%	−5.3%

TABLE XI. Summary of the observed data samples: single proton, CCQE e-like and CCQE μ-like, for SK-I, SK-II.

Event class	SK-I data	SK-II data
NC elastic (expected NC elastic fraction)	27 (64.7%)	11 (55.6%)
CCQE e-like (expected CCQE fraction)	31 (53.0%)	16 (51.4%)
CCQE μ-like (expected CCQE fraction)	60 (62.4%)	18 (61.3%)

VI. CONCLUSION

We have developed a technique for identifying proton tracks in the Super-Kamiokande detector, relying on their distinctive Cherenkov ring pattern. The proton momentum threshold for Cherenkov radiation is 1.07 GeV/c, and above about 2 GeV/c they produce visible secondary particles through hadronic interactions in the water, which makes identification outside of this proton momentum range very difficult. Because of this we find that protons can be identified efficiently in the momentum range between 1.25 GeV/c and 1.7 GeV/c. The majority of atmospheric neutrino interactions produces protons with momenta below the Cherenkov threshold, which results in low statistics. Using the full SK-I and SK-II data sets (2285.1 days), we have applied this tool to identify neutral current elastic events. The combined data are compatible with the observation of protons ($\chi^2 = 9.3$ for 6 bins, $P = 15.7\%$).

In a separate analysis, we have selected a sample of CCQE events, reconstructing both the lepton and the proton, and thereby the incoming neutrino kinematic parameters. This is the first time that kinematic reconstruction of the neutrino track is reported in a water Cherenkov detector using atmospheric neutrinos. This sample has $91.7 \pm 3\%$ neutrino (as opposed to antineutrino) content, potentially allowing studies where separating neutrinos and antineutrinos is crucial, e.g. resolving the neutrino mass hierarchy. The technique reported in this paper has an angular resolution of 12° for ν_μ and 16° for ν_e on the neutrino track, allowing the observation of a clear zenith-angle dependent asymmetry in the neutrinos themselves. The observed up-down asymmetry using neutrino track reconstruction is -0.52 ± 0.17(stat) for μ-like events and -0.06 ± 0.24 for e-like events, compatible with our previous results with other higher energy samples and $\nu_\mu \rightarrow \nu_\tau$ neutrino oscillations.

Although the CCQE selection yields low statistics in Super-Kamiokande and is not competitive with previously published measurements of the oscillation parameters, we have performed a fit of the L/E distribution including relevant systematic effects. With this sample alone, the no-oscillation hypothesis is excluded at 3 standard deviations. Table XI summarizes the new data samples selected in this paper. We expect that this new technique will be of particular interest to future projects involving water Cherenkov detectors even larger than Super-Kamiokande, where the statistics will be much higher.

ACKNOWLEDGMENTS

We gratefully acknowledge the cooperation of the Kamioka Mining and Smelting Company. The Super-Kamiokande experiment was built and has been operated with funding from the Japanese Ministry of Education, Science, Sports and Culture, and the United States Department of Energy. We gratefully acknowledge individual support by the National Science Foundation, and the Polish Committee for Scientific Research. Some of us have been supported by funds from the Korean Research Foundation (BK21), the Korea Science and Engineering Foundation, and the Japan Society for the Promotion of Science, and Research Corporation.

[1] Y. Fukuda *et al.*, Nucl. Instrum. Methods Phys. Res., Sect. A **501**, 418 (2003).
[2] Y. Ashie *et al.* (Super-Kamiokande Collaboration), Phys. Rev. D **71**, 112005 (2005).
[3] J. F. Beacom and S. Palomares-Ruiz, Phys. Rev. D **67**, 093001 (2003).
[4] T. Barszczak, Ph.D. thesis, University of California, Irvine, 2005.
[5] S. Agostinelli *et al.* (GEANT4 Collaboration), Nucl. Instrum. Methods Phys. Res., Sect. A **506**, 250 (2003).
[6] F. James and M. Roos, Comput. Phys. Commun. **10**, 343 (1975).
[7] M. Shiozawa, Ph.D. thesis, University of Tokyo, Japan, 1999.
[8] E. Davies, *Machine Vision: Theory, Algorithms, Practicalities* (Academic, New York, 1997).
[9] M. Honda, T. Kajita, K. Kasahara, S. Midorikawa, and T. Sanuki, Phys. Rev. D **75**, 043006 (2007).
[10] Y. Hayato, Nucl. Phys. B, Proc. Suppl. **112**, 171 (2002).
[11] D. Casper, Nucl. Phys. B, Proc. Suppl. **112**, 161 (2002).

[12] R. Brun and F. Carminati, CERN Report No. W5013, 1993 (unpublished).
[13] J. Hosaka *et al.* (Super-Kamiokande Collaboration), Phys. Rev. D **73**, 112001 (2006).
[14] A. Hocker *et al.*, Proc. Sci., ACAT2007 (2007) 040 [arXiv: physics/0703039].
[15] S. Fukuda *et al.* (Super-Kamiokande Collaboration), Phys. Rev. Lett. **85**, 3999 (2000).
[16] C. W. Walter (Super-Kamiokande Collaboration), Nucl. Instrum. Methods Phys. Res., Sect. A **503**, 110 (2003).
[17] G. L. Fogli, E. Lisi, and A. Marrone, Phys. Rev. D **63**, 053008 (2001).
[18] Y. Ashie *et al.* (Super-Kamiokande Collaboration), Phys. Rev. Lett. **93**, 101801 (2004).
[19] W.-M. Yao *et al.* (Particle Data Group), J. Phys. G **33**, 1 (2006).
[20] Y. Fukuda *et al.* (Super-Kamiokande Collaboration), Phys. Rev. Lett. **81**, 1562 (1998).
[21] M. C. Sanchez *et al.* (Soudan 2 Collaboration), Phys. Rev. D **68**, 113004 (2003).